2023 IEEE International Conference on Robotics and Automation (ICRA 2023)
May 29 - June 2, 2023. London, UK

Design and Control of a Tunable-Stiffness Coiled-Spring Actuator

Shivangi Misra, Mason Mitchell, Rongqian Chen and Cynthia Sung

***Abstract*— We propose a novel design for a lightweight and compact tunable stiffness actuator capable of stiffness changes up to 20x. The design is based on the concept of a coiled spring, where changes in the number of layers in the spring change the bulk stiffness in a near linear fashion. We present an elastica nested rings model for the deformation of the proposed actuator and empirically verify that the designed stiffness-changing spring abides by this model. Using the resulting model, we design a physical prototype of the tunable-stiffness coiled-spring actuator and discuss the effect of design choices on the resulting achievable stiffness range and resolution. In the future, this actuator design could be useful in a wide variety of soft robotics applications, where fast, controllable, and local stiffness change is required over a large range of stiffnesses.**

I. Introduction

Tunable compliance devices are a popular choice for the actuation of soft robots. The ability to actively control compliance or stiffness of a soft robot gives the robot extra degrees of freedom that it can use to achieve higher efficiency behaviors [1], [2]. For example, in legged robots, leg compliance varied periodically in synchrony with gait cycle ensures energy efficiency over long intervals of activity [3]. In surgical continuum arms, precision at the site of the operation can be achieved by stiffening the manipulator body without losing compliance elsewhere in the body [4]. Similarly, gripper arms match the compliance of the object being grasped to prevent it from harm due to the application of excessive force [5], [6]. In all of these applications, the ability of the robot to change its local stiffness and the stiffness distribution over its body is key.

At the same time, however, current tunable stiffness actuators are for the most part unable to achieve the combination of large stiffness change and precision control required for these applications [7], [8]. Popular approaches involving materials-level response [9], [10] through phase change [11], [12], response to magnetic fields [13], [14], [15], or electrostatic forces [16], [17], for example, are able to achieve large stiffness ranges on the order of 100 times [18]. They can be easily embedded into a robot skin to enact local stiffness changes without restricting continuous deformation. However, these actuators often exhibit only binary hard-soft behaviors and are thus difficult to use for fine-grain control. On the other hand, mechanism-based approaches involving pneumatically inflatable structures [19], [20], tendon-driven designs [21], [22], or auxetics and other metamaterials [23], [24], [25], [26], [27] are able to achieve precise stiffness control, but at the cost of bulky hardware, undesired shape changes, or low stiffness ranges. Among these mechanisms, jamming approaches [28], [29] are able to achieve large stiffness changes with relatively low volume, but are largely binary actuators, thus again sacrificing controllability.

We propose a novel, light-weight tunable-stiffness spring mechanism that produces controllable and continuous stiffness changes of up to 20x. The design is based on the concept of a coiled ribbon of flexible material, where real-time stiffness variation is achieved by altering the number of layers of the coil. We demonstrate that the proposed actuator can achieve a large range of discrete stiffness values with a resolution that can be configured by choice of material used. The proposed actuator outperforms material-based approaches in speed of response. It has an advantage over pneumatic devices in being lightweight and available for use in untethered robots. It can also be easily powered by off-the-shelf batteries and precisely controlled. An added advantage is that the stiffness change within the spring does not induce a shape or geometry change unlike many of the prevalent approaches. The combination of all these qualities make it a promising strategy for affecting stiffness change in future soft or compliant systems. In particular, the main contributions of this paper are:

- a lightweight, fast, tunable-stiffness coiled spring mechanism capable of real-time, designable stiffness changes,
- a model of our tunable-stiffness actuator based on nested elastic rings,
- two design variations of the proposed actuator that present trade-offs in stiffness range vs. actuator volume,
- hardware prototypes and evaluation of proposed tunable stiffness spring, and
- a demonstration of how multiple actuators can be combined and jointly controlled in the context of a manipulator application.

The remainder of this paper is structured as follows: Section II describes the underlying model for our actuator, the nested ring model. Section III discusses the design of the tunable-stiffness spring and how stiffness is controlled. Section IV includes experimental results, potential design variations, and discussion of the performance of the proposed tunable-stiffness spring. Section V concludes with directions for future work.

Support for this project has been provided in part by NSF Grants No. 1845339 and 1950720, and by the Johnson & Johnson WiSTEM2D Scholars Program. The authors would also like to thank Ruchi Gupte for help with initial exploration and Jeremy Wang for fabrication assistance.

S. Misra, R. Chen, and C. Sung are with the General Robotics, Automation, Sensing & Perception (GRASP) Lab at the University of Pennsylvania, Philadelphia, PA, USA. M. Mitchell is with the Soft Robotics Lab, Worcester Polytechnic Institute, Worcester, MA, USA. {shivangi, willchan, crsung}@seas.upenn.edu, mdmitchell@wpi.edu

2023 IEEE International Conference on Robotics and Automation (ICRA) | 979-8-3503-2365-8/23/$31.00 ©2023 IEEE | DOI: 10.1109/ICRA48891.2023.10161218

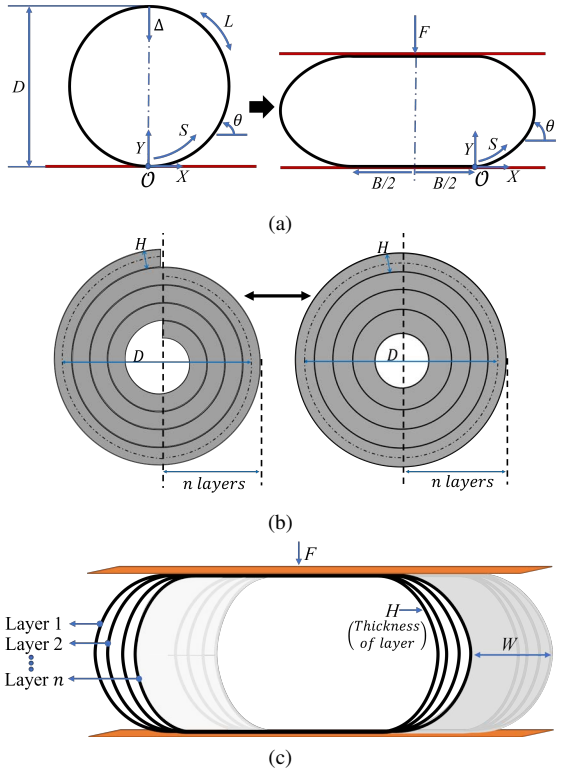

Fig. 1. (a) 2-D representation of single elastic ring with model variables indicated; shown in unloaded form (left) and with plate load F (right). (b) Coiled ribbon (left) with diameter of centerline D, thickness H and number of layers n shown in 2-D. We model the ribbon as n nested rings (right). (c) 3-D visualization of n nested cylinders of thickness H and width W under plate loading.

II. Coiled Spring Model

Our proposed tunable stiffness actuator is a plastic coiled tape spring with a variable number of layers. By controlling the number of layers in the coil, the bulk stiffness of the spring can be increased or decreased in a near-linear fashion, as predicted by mechanics theory in beam bending. In this section, we describe our model for the variable stiffness coiled-tape actuator design, starting first with the model for a single ring, and then extending the model to multiple layers.

A. Single Ring Compression Model

Consider first a single elastic ring of diameter D and width W as depicted in Fig. 1. The ring has a Young's Modulus E, cross-sectional moment of inertia $I = WH^3/12$, and total arc length $L = D\pi$. The ring sits on a flat rigid surface. We are interested in the deformation of this ring when a plate load F is applied at the top.

We use the model in [30], [31] to analyze this system. Let S be the arc length parameter that we use to indicate a location on the ring. We define $S = 0$ to be the rightmost point on the ring that is still in contact with the bottom plate, with S increasing counterclockwise. Then the coordinates of the ring $X(S)$ and $Y(S)$ and its angle $\theta(S)$ from horizontal are functions of the arc length parameter. The origin of the coordinate system is such that $X(0) = Y(0) = 0$. When a loading force F is applied, the ring is compressed by a total distance Δ in the vertical direction. This compression generates internal bending moments $M(S)$, horizontal forces $P(S)$, and vertical forces $Q(S)$, which dictate the change in $X(S), Y(S)$ along the arc length.

Using this parameterization, it is possible to nondimensionalize the system for simpler analysis according to

$$x = \frac{X}{L},\ y = \frac{Y}{L},\ s = \frac{S}{L},\ \delta = \frac{\Delta}{L}$$
$$f = \frac{FL^2}{EI},\ p = \frac{PL^2}{EI},\ q = \frac{QL^2}{EI},\ m = \frac{ML}{EI} \tag{1}$$

In this case, the nondimensionalized arc length parameter $s \in [0, 1]$ and the geometry of the system is determined by

$$\frac{\partial x}{\partial s} = \cos\theta,\ \frac{\partial y}{\partial s} = \sin\theta \tag{2}$$

To model the deformation of the ring, there are then two cases to consider. For small loads f, the change in curvature can be computed using an elastica model [30], [32], [33]:

$$\frac{\partial \theta}{\partial s} = m + 2\pi \tag{3}$$
$$\frac{\partial m}{\partial s} = \frac{f}{2}\cos\theta - p\sin\theta \tag{4}$$

where the term 2π on the right-hand side of Eq. (3) indicates that the ring's natural state in the absence of loading ($m = 0$) is a circle.

For large loads f, parts of the ring flatten to conform to the compressive plates at the top and bottom (Fig. 1). Call the length of the ring that has flattened out $b = B/L$. Then the governing equations Eq. (3) and (4) hold for $s \in [0, 0.5 - b] \cup [0.5, 1 - b]$ and $\frac{\partial\theta}{\partial s} = 0$ otherwise. This condition can be detected when there exists a $\theta(s') = \pi$ that satisfies the moment-curvature equations with $s' < 0.5$, that is, that the ring flattens out before the midpoint of s. In this case, the point $s = 0$ no longer lies at the bottom center of the ring, and $b = 0.5 - s'$. It has been previously shown in [30] that $b > 0$ when $f > f_{crit} = 110.03$.

Figure 2 illustrates the resulting model for a nondimensionalized ring. The model equations were solved using shooting method with the following boundary conditions: For small loads with $f \leq f_{crit}$, initial boundary conditions $x(0) = y(0) = 0, \theta(0) = 0$ and final boundary conditions $x(0.5) = 0, \theta(0.5) = \pi$, with the constraint that $b = 0$. For large loads with $f > f_{crit}$, initial boundary conditions $x(0) = y(0) = 0, \theta(0) = 0, m(0) = -2\pi$ and final boundary conditions $x(0.5) = 0, \theta(0.5) = \pi$. The vertical compression of the ring was then computed as

$$\delta = \frac{1}{\pi} - y(0.5) \tag{5}$$

B. Coiled Spring Compression Model

For the coiled spring with multiple layers, we extend upon the single-ring model. We model the spiral coil as a set of nested concentric rings where the inner surface of one ring is always in contact with the outer surface of the ring inside it at their top and bottom-most points respectively. Then the individual layers of the coil can be treated as

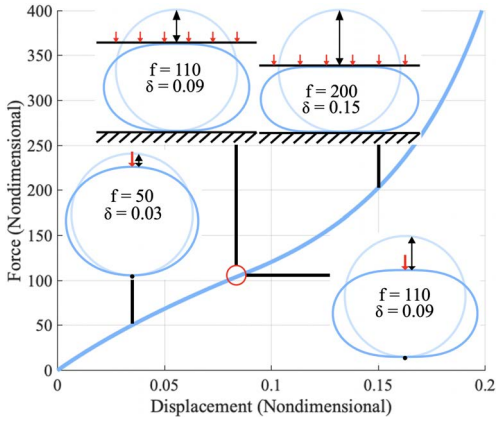

Fig. 2. Non-dimensionalized ring deformation curve with a force ranging from 0 to 400. Displacement (x-axis) goes up to non-dimensional $D = 1/\pi$, approximated as 0.2.

parallel springs with the same compressive deformation Δ but different diameters.

For a coil with n layers, modeled as n nested rings, number the rings $i \in \{0, 1, 2, \cdots, n-1\}$ with $i = 0$ being the outermost ring. Due to the thickness of the layers, the ith ring has diameter $D_i = D - 2iH$, where D is the outermost ring diameter and H is the material thickness. Then, for a given displacement Δ, the total force exerted by the compressive plate at the top of the coil is given by

$$F = \sum_{i=0}^{n-1} F_i \tag{6}$$

where F_i is the dimensionalized force computed using the single-ring model in Section II-A for each layer i.

C. Effective Stiffness of Coiled Spring

In the end, the goal of our design is to control the stiffness, not necessarily the deformation, of the spring. Starting with a single ring, we approximate the linearized stiffness as

$$K = \frac{F}{\Delta} = \frac{f}{\delta} \cdot \frac{EI}{L^3} = \frac{f}{\delta} \cdot \frac{EWH^3}{12\,(\pi D)^3} \tag{7}$$

Denote by $k = \frac{f}{\delta}$ the nondimensional stiffness for a single ring, and by $K^{(1)} = \frac{F}{\Delta}$ the corresponding dimensionalized stiffness. That is,

$$K^{(1)} = k\frac{EWH^3}{12(\pi D)^3} \tag{8}$$

For an n-layer coil, treated as n rings in parallel, the bulk stiffness is then

$$K^{(n)} = k\frac{EWH^3}{12\pi^3} \sum_{i=0}^{n-1} \frac{1}{(D - 2iH)^3} \tag{9}$$

D. Partial Layers

Note that unlike nested rings, our coiled spring concept is capable of generating partial layers, where the innermost layer of the coil is not a full circle. For the purposes of control, we estimate the stiffnesses of these configurations using linear interpolation. Practically, however, slip between the layers will likely affect the true stiffness of the structure.

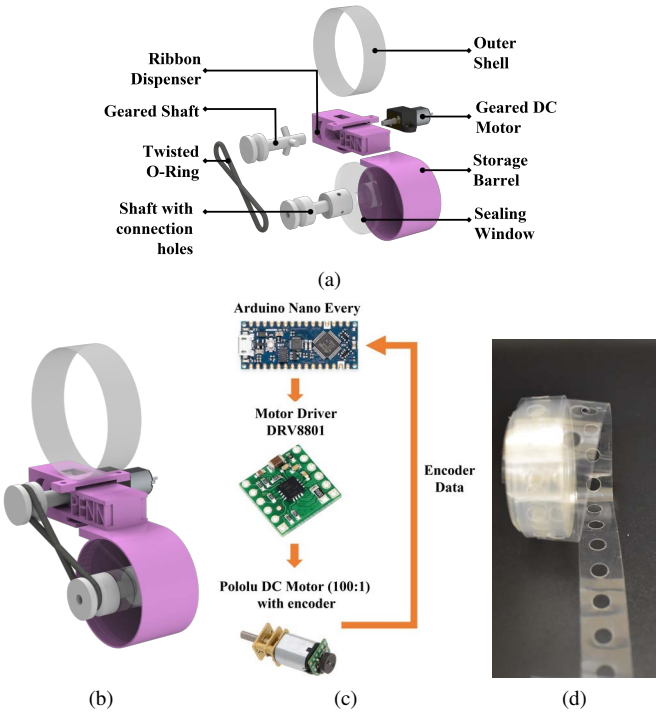

Fig. 3. (a) Exploded view of tunable stiffness actuator design. (b) Actuator CAD model. (c) Electronics. (d) Balloon tape for coiled spring.

III. Tunable Stiffness Coiled Spring Actuator

A. Design

We implemented the tunable-stiffness coiled spring concept in a physical actuated prototype shown in Fig. 3. The coiled spring itself consists of a 0.178 mm thick PET off-the-shelf balloon tape (non-adhesive, $E = 5.7$ GPa). The film is 15 mm wide with 6.35 mm holes every 12.7 mm. The coil is enclosed in a circular outer shell 50 mm in diameter and constructed from 0.254 mm thick PET film (Polyethylene terephtalate, McMaster 8567K92, $E = 2.8$ GPa). This ring was manufactured by cutting the film using a PLS4.75 CO2 laser cutter, then bending the resulting strip into ring shape and affixing it to the base with bolts. The spring is able to achieve any number of layers between 1 and 10, with the maximum amount limited by the length of balloon tape used.

The spring actively changes its own stiffness using a motor-driven base consisting of a ribbon dispenser and storage barrel. The ribbon dispenser controls the number of layers and drives excess material into the cylindrical barrel for compact storage. The ribbon dispenser is driven using a 12V 100:1 geared Pololu micro motor[1] attached to the geared shaft, which allows it to interface with the holes in the balloon tape. A twisted rubber O-ring drives a shaft through the storage barrel to actively spool the material at the same speed as the ribbon dispenser, driven by the motor. All parts of the base are 3D printed in PLA (Polylactic Acid) on a Prusa Mini[2] at 15% infill. The storage container is sealed

[1]https://www.pololu.com/product/3052/
[2]https://www.prusa3d.com/category/original-prusa-mini/

with a circular acrylic plate. The entire design, including base, weighs 52.7 g.

B. Stiffness Control

Active control of the actuator stiffness is achieved using proportional feedback control. The number of layers n^* corresponding to a desired stiffness $K^{(n^*)}$ can be found by solving Eq. (9) for n. For practical use, the computational load is eased by using Eq. (9) to construct a lookup table with increments of half layers. The lookup table is easily constructed and stored, as the actuator is only able to house a finite length of ribbon.

The desired number of layers is then converted to an equivalent length of coiled ribbon, L^*. Theoretically, this value could be computed as,

$$L^* = \int_0^{2\pi n^*} \left(\frac{D}{2} - \frac{\alpha}{2\pi} H \right) d\alpha = 2\pi n^* \frac{D}{2} - (n^*)^2 \pi H \tag{10}$$

which is the length of a spiral with an outer diameter D, thickness H, and number of layers n^*. As the current state of the actuator is tracked by a magnetic encoder (Pololu #4760), the desired state also uses encoder counts for each L^* to enable comparison. However, small gaps between successive layers, formed as the coil winds or unwinds, introduce errors in this conversion. To improve accuracy, we instead use empirically obtained encoder data to construct a lookup table for the value of the desired state, during both winding and unwinding operations. Finally, the controller minimizes the difference in current and desired states by proportionally altering the motor voltage via a PWM signal to its motor driver (Pololu DRV8801). The controller is implemented on an Arduino Nano Every board and the overall communication loop is shown in Fig. 3c.

IV. Experiments

A. Effect of Design Parameters and Model Validation

We first validate our model for an unactuated coiled spring to verify the effect of different design parameters on the experimental force-displacement curve. The outer shell and coiled tape of the spring samples were constructed with PET material and design parameters in Table I. An MTS Criterion (Series 40) machine with a 1 kN load cell was used to obtain the force-displacement curves of each spring sample as the number of layers was varied from 1 to 20 layers in half-layer steps. Each sample was compressed between two plates at a rate of 0.25 mm/s up to a maximum compression of 30 mm, which was determined experimentally as the maximum value without creasing the inner layers of the coil. Fig. 4a shows the results for a sample with $D = 50$ mm, $W = 10$ mm, $H = 0.127$ mm. The curves are approximately linear for compression amounts of up to 25 mm and become increasingly non-linear afterwards. It is also to be noted that for every increment in no. of coiled layers, the slope of the curves (up to 25 mm compression) scale almost linearly. Thus the spring is able to vary continuously in stiffness from as low as 0.003 N/mm at 1 layer to as high as 0.074 N/mm at 20 layers. Plots for all other coil samples looked similar in shape and trends across layers. We compared the experimental force-displacement data to the dimensionalized model. Model parameters were fit to the experimental data to minimize sum of squared error over all measured curves for the sample. The resulting fitted parameters (Table I) were within the tolerance of the nominal values reported by the manufacturers. The resulting error between experimental and theoretical data is shown as heat maps in Fig. 4b for each of the spring samples. These plots show relatively low error (less than 10%) during the first half of the total compression amount with error increasing thereafter. Deviations from theoretical predictions may be attributed to effects such as friction and gaps between layers.

TABLE I
Spring Samples: Parameter Sets

ID	W (mm), 10%		D (mm), 10%		H (mm), 10%		E (GPa), 1%	
	T	F	T	F	T	F	T	F
1	10.0	10.0	50.0	45.49	0.127	0.139	2.8	2.827
2	10.0	10.0	50.0	46.1	0.254	0.279	2.8	2.83
3	20.0	20.0	50.0	50.1	0.254	0.279	2.8	2.828
4	10.0	10.0	70.0	64.9	0.254	0.270	2.8	2.77

Column headings formatted as "parameter (unit), tolerance%"
T: theoretical value, F: fitted value

B. Actuation and Control

We tested our actuated prototype's ability to generate consistent controlled stiffnesses using the ribbon dispenser design in Section III. We used a P-controller with gain $k_p = 1.75$ (PWM units/count), obtained via trial-and-error, to vary the number of layers of the tunable-stiffness coiled spring actuator from 1 to 10 in half layer increments. The actuated spring was able to successfully produce the desired number of layers for all cases. With these parameters, the controller had a mean positional error of 4.3 mm (standard deviation of 2.16 mm). These error measurements were collected by finding the arc length distance between achieved position of the inside end of the coiled ribbon and its corresponding desired position. On average, the motor took approximately 1 s to wind or unwind a whole layer. To measure the resulting stiffness, we used the same procedure as in Section IV-A. The experimental setup and force-displacement plots are shown in Fig. 5. We find that the actuated spring also displays an approximately linear trend in stiffness with increasing number of layers, with a total stiffness gain of approximately $3.5\times$, from 0.036 N/mm to 0.125 N/mm. The base initial stiffness is due to the outer shell and there is subsequently a $9\times$ finer stiffness gain due to inner layers.

C. Double-Loop Spring: a Design Variation

The actuator stores extra tape inside a storage barrel, which takes up volume. For some applications requiring closely integrated springs, this might be undesirable. Therefore, we designed a variation with a second lower loop instead of a storage unit, shown in Fig. 6. The tape from the upper coil is channelled into the lower coil and vice versa using the motor-gear setup. As a result, there is always

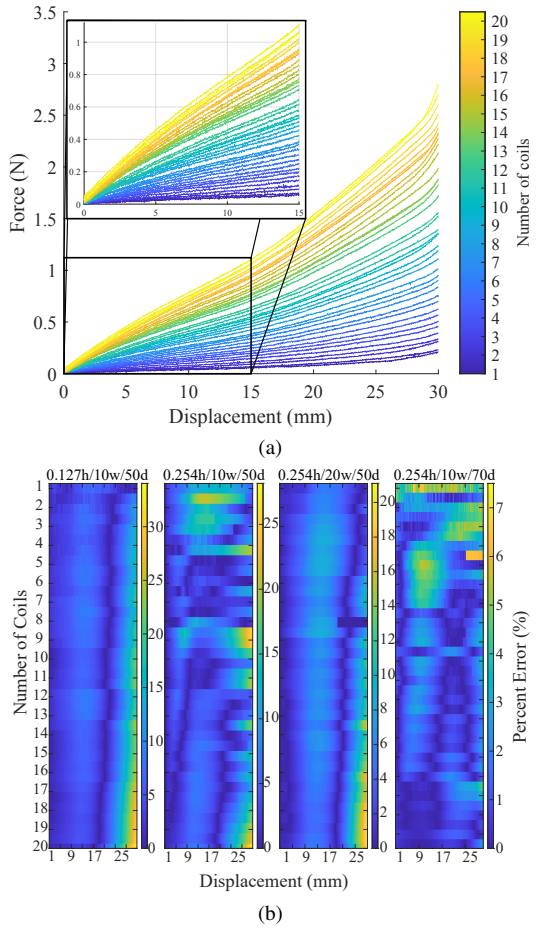

Fig. 4. (a) Experimental MTS test for spring ($H = 0.127$ mm, $W = 10$ mm, $D = 50$ mm) over a range of 1-20 coils with a total compression amount of 30 mm. (b) Error plots for MTS experiments run with spring sample: Sample ID 1-4 (from left to right).

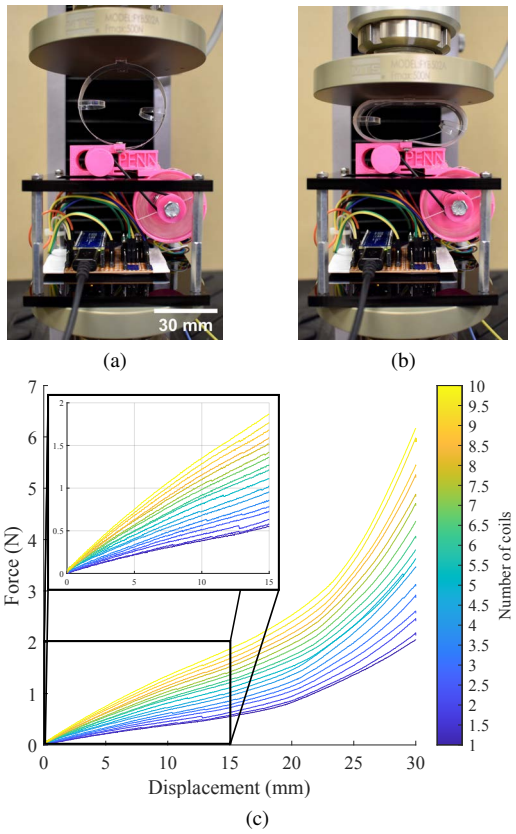

Fig. 5. (a) Experimental MTS test for an actuated tunable stiffness spring ($D = 50$ mm, $W = 15$ mm, $H = 0.178$ mm) (b) A PID controller used to add 7 inner layers to the actuated spring in (a); followed by a compression of 25 mm. The outer shell has loops to retain coiled layers within the spring. (c) Experimental force-displacement curves for actuated spring with layers between 1 to 10, in half-layer steps.

a complementary number of layers in the upper and lower loops. The effective stiffness of such a spring is calculated by treating the upper and lower loop as springs in series.

We constructed a prototype of this double-loop spring where both upper and lower loops have parameters $D = 50$ mm, $W = 15$ mm, an outer layer of 0.254 mm PET ($E = 2.8$ GPa), 9 inner coiled layers each of 0.178 mm balloon tape with $E = 5.2$ GPa. Fig. 6b shows the design and the force-displacement curves obtained by varying layers in the upper loop from 1 to 10 in half-layer increments. Due to the symmetry of the spring, lower loop tests were not required. From the plots, we see that the maximum force generated by the prototype is half that of the single-loop actuator. This is as expected for identical springs in series (when both loops have 10 total layers). The overall achievable stiffness gain with this spring is $1.7\times$. Between the single and double-loop designs, there is a trade-off between space-saving and the achievable stiffness gain for the same length of tape.

D. Application: Manipulator

Tunable stiffness actuators provide additional degrees of freedom to soft manipulators. In our final experiment, we built the 3 DOF manipulator shown in Fig. 7 by arranging four parallel tunable stiffness single-loop springs in a square connected with a plate on the top and bottom. We refer to the center of its top plate as the end-effector. A motor-driven tendon connected to the end-effector controls the extension of the manipulator. The spring modules were all controlled with an Arduino Nano Every, and the tendon via a DC motor with an L298N motor driver and an Arduino Uno microcontroller.

We estimate the reachable workspace of the manipulator by tracking its end-effector in an OptiTrack Motion Capture system. The stiffnesses of the springs were varied to extreme ends in all possible combinations, and the tendon was pulled until the module was compressed fully. We define "full" spring compression as 25 mm for springs of $D = 50$ mm, due to the favorable linear force-displacement profile in this region. The data collected is shown in Fig. 7c and Fig. 7d. The workspace is widest at a height of 12.5 mm with max height of 25 mm and a max radius of around 3 mm. The shape of the workspace is typical of continuum manipulators.

We also use the system to track square and circle shaped paths with the end-effector of the manipulator. Fig. 8 shows the results when the tendon is pulled by a length of 12.5 mm. The stiffness control algorithm from [34] was used to generate a sequence of desired stiffnesses for each of the

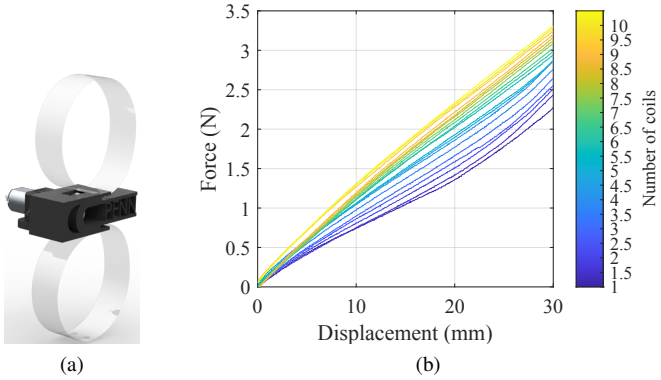

Fig. 6. (a) Double loop coiled spring design. (b) Experimental force-displacement curves for double-loop actuator with layers between 1 to 10, in half-layer steps.

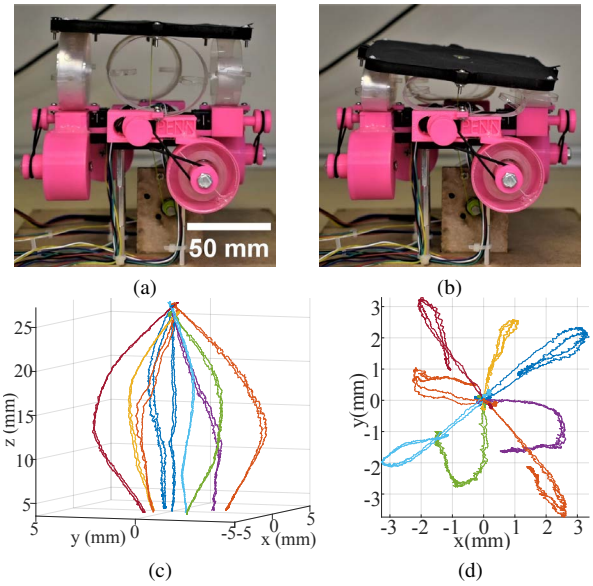

Fig. 7. (a) Manipulator in neutral position. (b) Inclined manipulator. (c) Side and (d) top view of the estimated workspace.

four springs. These desired stiffnesses were translated to the desired number of coiled layers using the steps described in Section III-B and are plotted in Fig. 8. The manipulator tracks each path with an RMSE error of 0.12 mm and 0.081 mm for the square and circle respectively. The paths taken by the manipulator end-effector are noisy due to vibrations in changing the number of layers. In addition, the square and circle paths do not have closed shapes, likely because of slip between the coil layers. In the future, closed loop position feedback between the motion capture system and the manipulator would address this error.

V. Conclusion

In this paper we introduce a design for a novel tunable stiffness actuator that is fast, lightweight, and can be utilized for millimeter accurate use in complex soft mechanisms. The underlying concept involves using a coiled film as a strategy to attain simple tunable stiffness structures. We detail

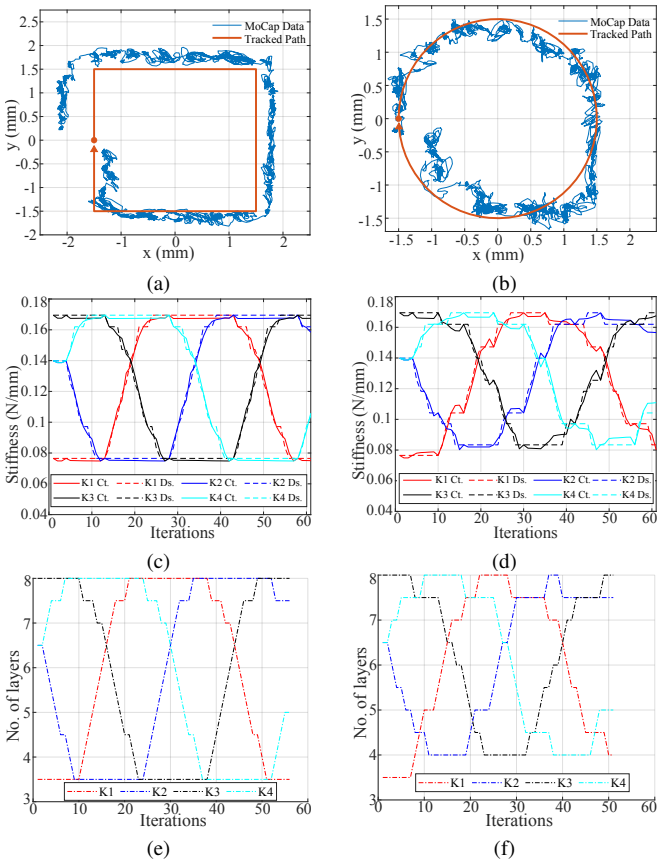

Fig. 8. Tracking tests for (a) a square of side length 3 mm and (b) a circle of radius 1.5 mm in 61 steps (approximately 1.5 minutes). (c/d) desired continuously (Ct.) varying stiffnesses and corresponding closest discrete (Ds.) stiffness that are achievable by the springs ($K1, K2, K3, K4$) for the square and circle tests, respectively. (e/f) layer changes in square and circle tests, respectively.

how this concept translates into a tunable stiffness actuator, implemented using off-the-shelf motors, plastic films, and 3D printed parts, and we verify its functionality through a number of force-displacement measurements.

The proposed tunable-stiffness coiled-spring actuator can theoretically achieve any amount of stiffness gain, depending on the number of layers that can be coiled in its outer shell. This is only limited by the diameter of the outer shell, thickness of ribbon material and friction created between layers. Additionally, it is possible to scale the spring and accompanying model to suit different applications. The spring can be used in un-tethered robots and can also house sensors. A shortcoming of this work is that we do not model cases when the spring bends out-of-plane due to compression by inclined plates. This type of deformation is present in our compliant manipulator and may impact the effective stiffness of the spring. We intend to address these limitations in the future by extending the mathematical model to accommodate such cases. We will also improve upon the actuator design by reducing friction between the layers for larger stiffness gains, reducing weight and volume, and including sensing to predict the deformation and real-time stiffness of the spring.

REFERENCES

[1] J. L. C. Santiago, I. S. Godage, P. Gonthina, and I. D. Walker, "Soft robots and kangaroo tails: Modulating compliance in continuum structures through mechanical layer jamming," *Soft Robotics*, vol. 3, no. 2, pp. 54–63, 2016.

[2] S. L. Hooper, "Motor control: The importance of stiffness," *Current Biology*, vol. 16, no. 8, pp. R283–R285, 2006.

[3] K. C. Galloway, J. E. Clark, and D. E. Koditschek, "Variable Stiffness Legs for Robust, Efficient, and Stable Dynamic Running," *Journal of Mechanisms and Robotics*, vol. 5, no. 1, 01 2013, 011009.

[4] L. Blanc, A. Delchambre, and P. Lambert, "Flexible medical devices: Review of controllable stiffness solutions," *Actuators*, vol. 6, no. 3, 2017.

[5] C. Majidi, "Soft robotics: A perspective—current trends and prospects for the future," *Soft Robotics*, vol. 1, no. 1, pp. 5–11, 2014.

[6] M. Giannaccini, I. Georgilas, I. Horsfield, B. Peiris, A. Lenz, and S. Dogramadzi, "A variable compliance, soft gripper," *Autonomous Robots*, vol. 36, 12 2013.

[7] M. Manti, V. Cacucciolo, and M. Cianchetti, "Stiffening in soft robotics: A review of the state of the art," *IEEE Robotics Automation Magazine*, vol. 23, no. 3, pp. 93–106, 2016.

[8] L. Blanc, A. Delchambre, and P. Lambert, "Flexible medical devices: Review of controllable stiffness solutions," *Actuators*, vol. 6, no. 3, 2017.

[9] B. Ma, M. Z. Shaqura, R. C. Richardson, and A. A. Dehghani-Sanij, "A study on phase-changing materials for controllable stiffness in robotic joints," *Robotics*, vol. 11, no. 3, 2022.

[10] J. Peters, E. Nolan, M. Wiese, M. Miodownik, S. Spurgeon, A. Arezzo, A. Raatz, and H. A. Wurdemann, "Actuation and stiffening in fluid-driven soft robots using low-melting-point material," in *2019 IEEE/RSJ International Conference on Intelligent Robots and Systems (IROS)*, 2019, pp. 4692–4698.

[11] Y. Kim, S. S. Cheng, and J. P. Desai, "Active stiffness tuning of a spring-based continuum robot for mri-guided neurosurgery," *IEEE Transactions on Robotics*, vol. 34, no. 1, pp. 18–28, 2018.

[12] M. Cianchetti, M. Calisti, L. Margheri, M. Kuba, and C. Laschi, "Bioinspired locomotion and grasping in water: the soft eight-arm OCTOPUS robot," *Bioinspiration & Biomimetics*, vol. 10, no. 3, p. 035003, may 2015.

[13] C. Cao and X. Zhao, "Tunable stiffness of electrorheological elastomers by designing mesostructures," *Applied Physics Letters*, vol. 103, no. 4, p. 041901, 2013.

[14] C. Majidi and R. J. Wood, "Tunable elastic stiffness with microconfined magnetorheological domains at low magnetic field," *Applied Physics Letters*, vol. 97, no. 16, p. 164104, 2010.

[15] Y. Li, J. Li, W. Li, and H. Du, "A state-of-the-art review on magnetorheological elastomer devices," *Smart Materials and Structures*, vol. 23, no. 12, p. 123001, nov 2014.

[16] M. Henke, J. Sorber, and G. Gerlach, "Multi-layer beam with variable stiffness based on electroactive polymers," in *Electroactive Polymer Actuators and Devices (EAPAD) 2012*, vol. 8340, International Society for Optics and Photonics. SPIE, 2012, p. 83401P.

[17] R. Pelrine and R. Kornbluh, "Variable-stiffness–mode dielectric elastomer devices," *Advances in Science and Technology*, vol. 61, pp. 192–201, 09 2008.

[18] J. Shintake, B. Schubert, S. Rosset, H. Shea, and D. Floreano, "Variable stiffness actuator for soft robotics using dielectric elastomer and low-melting-point alloy," in *2015 IEEE/RSJ International Conference on Intelligent Robots and Systems (IROS)*, 2015, pp. 1097–1102.

[19] M. S. Xavier, C. D. Tawk, A. Zolfagharian, J. Pinskier, D. Howard, T. Young, J. Lai, S. M. Harrison, Y. K. Yong, M. Bodaghi, and A. J. Fleming, "Soft pneumatic actuators: A review of design, fabrication, modeling, sensing, control and applications," *IEEE Access*, vol. 10, pp. 59 442–59 485, 2022.

[20] C. Xiang, M. E. Giannaccini, T. Theodoridis, L. Hao, S. Nefti-Meziani, and S. Davis, "Variable stiffness mckibben muscles with hydraulic and pneumatic operating modes," *Advanced Robotics*, vol. 30, no. 13, pp. 889–899, 2016.

[21] D. Zappetti, R. Arandes, E. Ajanic, and D. Floreano, "Variable-stiffness tensegrity spine," *Smart Materials and Structures*, vol. 29, 2020.

[22] P. M. Loschak, S. F. Burke, E. Zumbro, A. R. Forelli, and R. D. Howe, "A robotic system for actively stiffening flexible manipulators," in *2015 IEEE/RSJ International Conference on Intelligent Robots and Systems (IROS)*, 2015, pp. 216–221.

[23] Z. Zhai, Y. Wang, K. Lin, L. Wu, and H. Jiang, "In situ stiffness manipulation using elegant curved origami," *Science Advances*, vol. 6, no. 47, p. eabe2000, 2020.

[24] X. Cheng, Y. Zhang, X. Ren, D. Han, W. Jiang, X. G. Zhang, H. C. Luo, and Y. M. Xie, "Design and mechanical characteristics of auxetic metamaterial with tunable stiffness," *International Journal of Mechanical Sciences*, vol. 223, p. 107286, 2022.

[25] Y. Yuan and C. Sung, "Programmable Stiffness and Applications of 3D Printed TPU Grid Lattices," vol. 8A: 45th Mechanisms and Robotics Conference (MR), 08 2021.

[26] H. Yuan, J. Pikul, and C. Sung, "Programmable 3-d surfaces using origami tessellations," in *7th International Meeting on Origami in Science, Mathematics, and Education*, 2018, pp. 893–906.

[27] W.-H. Chen, S. Misra, Y. Gao, Y.-J. Lee, D. E. Koditschek, S. Yang, and C. R. Sung, "A programmably compliant origami mechanism for dynamically dexterous robots," *IEEE Robotics and Automation Letters*, vol. 5, no. 2, pp. 2131–2137, 2020.

[28] M. Ibrahimi, L. Paternò, L. Ricotti, and A. Menciassi, "A layer jamming actuator for tunable stiffness and shape-changing devices," *Soft Robotics*, vol. 8, no. 1, p. 85 – 96, 2021.

[29] L. Blanc, A. Pol, B. François, A. Delchambre, P. Lambert, and F. Gabrieli, "Granular jamming as controllable stiffness mechanism for medical devices," *Trends in Mathematics*, p. 57 – 66, 2018.

[30] L. N. Virgin, J. V. Giliberto, and R. H. Plaut, "Deformation and vibration of compressed, nested, elastic rings on rigid base," *Thin-Walled Structures*, vol. 132, pp. 167–175, 2018.

[31] C. Y. Wang, "Crushing of an Elastic-Perfectly Plastic Ring or Tube Between Two Planes," *Journal of Applied Mechanics*, vol. 54, no. 1, pp. 159–164, 03 1987.

[32] R. Plaut, J. Sidbury, and L. Virgin, "Analysis of buckled and pre-bent fixed-end columns used as vibration isolators," *Journal of Sound and Vibration*, vol. 283, no. 3, pp. 1216–1228, 2005.

[33] R. H. Plaut and L. N. Virgin, "Deformation and vibration of upright loops on a foundation and of hanging loops," *International Journal of Solids and Structures*, vol. 51, no. 18, pp. 3067–3075, 2014.

[34] S. Misra and C. Sung, "Forward kinematics and control of a tunable-stiffness 3-d continuum manipulator," *IEEE International Conference on Robotics and Automation (ICRA)*, 2022.